Role of Q-carbon in nucleation and formation of continuous diamond film

J. Narayan^{1,*}, A. Bhaumik², S. Gupta², P. Joshi¹, P. Riley¹, and R. J. Narayan^{2,3}

¹Department of Materials Science and Engineering, North Carolina State University, Raleigh, North Carolina 27695-7907, USA.

² Intel Corporation, Rolner Acres Campus 3, OR, 97124, USA.

³ Joint Department of Biomedical and Engineering, North Carolina State University and UNC Chapel Hill, Raleigh, North Carolina 27695-7907, USA.

^{*}Corresponding author, Tel: 919-515-7874, E-mail: narayan@ncsu.edu (J. Narayan)

Abstract

Formation of continuous and adherent diamond films on practical substrates presents a formidable challenge due to lack of diamond nucleation sites needed for diamond growth. This problem has been solved through the formation of interfacial Q-carbon layers by nanosecond laser melting of carbon layers in a highly undercooled state and subsequent quenching. The Q-carbon layer provides ready nucleation sites for epitaxial films on planar matching substrates such as sapphire, and polycrystalline films on amorphous substrates such as glass. Each laser pulse converts about a one-cm-square area, which can be repeated with a 100-200 Hz laser to produce potentially 100-200 cm²s⁻¹ of diamond films. This is essentially a low-temperature processing, where substrate stays close to ambient temperature, because the total heat input is quite small. The Q-carbon layer is also responsible for improved adhesion of diamond films on sapphire and glass substrates. It is also argued that the formation of Q-carbon layer is also responsible for efficient diamond nucleation during negatively biased MPCVD diamond depositions.

Keywords: Continuous epitaxial diamond film; Diamond nucleation and growth; Adhesion of diamond film.

1. Introduction

Efficient nucleation is critical for the growth of continuous diamond thin films needed for nextgeneration solid-state systems ranging from cutting tools to high-power and high-frequency devices to biosensing applications [1-3]. Both under hot-filament CVD (HFCVD) and microwave plasma CVD (MPCVD), diamond nucleation can be enhanced by external nanodiamond seeding, scratching, interposing layers, laser treating, and ion implantation with some success [1,2,4]. However, uniform nucleation of diamond still presents a formidable challenge to efficient growth and formation of heterostructures with continuous diamond films. Our recent breakthrough showed that new phase of Q-carbon formed by nanosecond laser processing can provide very uniform and efficient nuclei for diamond growth both under laser processing and subsequent hotfilament CVD (HFCVD) [5]. In the presence of a plasma, such as MPCVD, negative biasing prior to a subsequent growth cycle was shown to be quite efficient on Si(100) substrates, where diamond nuclei were found to be random [6]. Subsequently detailed studies on bias-enhanced nucleation (BEN) on Si(100) showed that the formation of an amorphous carbon layer played a critical role in enhancing the diamond nucleation density by over five orders of magnitude [7]. This amorphous carbon layer formed on the top of an amorphous SiC layer, but SiC layer by itself was found to be ineffective in enhancing the diamond nucleation density. As a result of amorphous nature of interposing SiC layer, these diamond films were polycrystalline with a random texture. The BEN processing generated considerable more excitement when Sawabe and colleagues reported that diamond thin films on Ir(100) substrate can be highly textured, close to epitaxial despite a 7.1% lattice misfit with diamond [8]. This promise of BEN for wafer-scale diamond epitaxy intrigued many researchers and led to studies on the underlying mechanism of diamond nucleation and epitaxy. Since BEN involved amorphous carbon layer in the diamond nucleation on Ir(100), the

source for diamond epitaxy was not clear. Schreck et al. reported domain formation during BEN on Ir(001) surfaces in the form of bright areas of several microns in diameter [9]. When MPCVD growth step was applied after BEN, epitaxially oriented diamond islands grew only within the domains. Outside the domains the nucleation density was found to be orders of magnitude lower and the diamond crystallites were found to be completely random. Despite this observation, the mechanisms of domain formation and nucleation enhancement remained elusive. Recently, Schreck et al. introduced ion-bombardment induced lateral growth of these domains, where they argued that this ion-bombardment-induced layer can provide nuclei which subsequently grow under unbiased growth conditions [10]. This layer contained domains which grew in circles and these domains contained a high sp³ fraction with some diamond structures, formed by ion bombardment, as revealed by X-ray photoelectron diffraction. However, this layer could not be characterized by HRTEM and did not show any crystalline diamond features either by imaging or electron diffraction, and the layer was too thin for Raman studies. In this model, the growth rates needed to account for observed domain sizes of the order of a few microns required excessive displacement damage [10]. The formation of circular domains regions has been also observed recently on Si(100) substrates after BEN using MPCVD [11].

The purpose of this paper is to show that these circular domains, formed under low-energy ion bombardment in solid state, are similar to circular Q-carbon regions formed during pulsed laser melting with high undercooling and quenching [12-14]. These Q-carbon regions represent a separate phase of carbon with distinct structure and entropy. It is shown that the Q-carbon phase consists of a high-density of tetrahedra that are packed randomly in an amorphous structure with high (>80%) sp³ content, as determined by electron diffraction and electron-energy-loss spectroscopy. Under laser processing, the resulting Q-carbon phase has been found to provide a

higher nucleation density for diamond, particularly near the substrate interface due to higher undercooling and lower Gibbs free energy. These Q-carbon nucleation sites can be used to achieve wafer-scale integration of epitaxial diamond films by introducing a laser processing treatment prior to HFCVD or MPCVD. If the diamond nucleation originates at the interface, then the diamond film can grow epitaxially, despite the large lattice misfit, following the principles of domain matching epitaxy [15], similar to diamond epitaxy on (001) iridium that involves a 7.1% tensile misfit. On amorphous substrates, such as glass, Q-carbon provides efficient nucleation for the formation of polycrystalline continuous diamond films.

2. Experimental

To form Q-carbon, we start with pulsed laser deposition of amorphous carbon (~500 nm) on c-sapphire substrates near room temperature. The operating pressure of the vacuum chamber was 1.0×10^{-6} to 5.0×10^{-7} Torr. Nanosecond laser pulses of KrF excimer laser (λ =248 nm, τ =25 ns) were used to ablate the amorphous carbon target mounted in the PLD chamber. The repetition rate and the range of laser energy density of the nanosecond laser were 10 Hz and 3.0-3.5 Jcm⁻², respectively. The ratio of sp² to sp³ bonded carbon in the as-deposited amorphous carbon thin films was controlled by selection of laser and substrate variables, including substrate temperature, pulse energy density, and laser plume characteristics. Following the PLD process, the amorphous carbon films were laser annealed using a nanosecond ArF excimer laser (λ =193 nm, τ =20 ns). The laser energy density used during the pulsed laser annealing (PLA) ranged from 0.6-1.0 Jcm⁻², and the laser pulse repetition rate varied from 10-200Hz. The PLA technique melted the amorphous carbon into a highly undercooled state of molten carbon and subsequently quenched the melt to form either Q-carbon, diamond, or α -carbon depending on the degree of undercooling. The Q-carbon is formed at the highest undercooling when a laser energy density ranging from 0.6-0.7 Jcm⁻² was

used. Diamonds and α -carbon were formed after the PLA of amorphous carbon with laser energy densities in the range of 0.7-1.0 Jcm⁻². With the increase in the laser energy density, there was a decrease in the degree of undercooling, which facilitated the formation of the diamond (from amorphous carbon). When laser energy densities exceeded 1.0 Jcm⁻² graphene formation was observed. It should also be noted that the degree of undercooling was dependent on the laser parameters and thermal conductivity of the substrate and the as-deposited thin film. Therefore, the laser parameters for the formation of Q-carbon and diamond differed for different substrates. Nucleation and growth rates determined the formation of nano- and micro-structures of diamond. The characterization of the Q-carbon and diamonds were performed by using high-resolution scanning electron microscopy (HRSEM), (scanning) transmission electron microscopy (STEM and TEM), core-loss EELS, electron dispersive X-ray spectroscopy (EDS), Raman spectroscopy, and electron backscatter diffraction (EBSD). The HRSEM was performed in the emission mode (having a sub-nanometer resolution) using FEI Verios 460L SEM. The Raman measurements were made using the Alfa300 R superior confocal Raman spectroscope (lateral resolution < 200 nm) with a 532 nm excitation source. The Raman spectrometer was calibrated using a standard crystalline Si sample, which had a vibrational mode (Raman peak) at 520.6 cm⁻¹. The EBSD measurements were performed in the FEI Quanta 3D FEG microscope using an EBSD HKL Nordlys detector. The lateral resolution of the EBSD detector (< 10 nm) enabled the Kikuchi mapping of microdiamonds, which provided the details of structure and relative orientation of the film with respect to the substrate.

3. Results and discussions

Amorphous carbon layers can be melted into a super undercooled state by using nanosecond laser pulses, and then converted upon quenching into diamond-like amorphous carbon with $\sim 60\%$ sp³

bonding (α -carbon), pure diamond, or a new phase of Q-carbon (with >80% sp³ bonding). The formation of these phases depends upon the degree of undercooling, where the undercooling increases from α -carbon to diamond to Q-carbon [12-14]. Fig. S1 shows schematically the formation of diamond, Q-carbon + α -carbon, and Q-carbon + diamond. The Q-carbon is formed near the sapphire substrate, where the undercooling is the highest and is followed by the formation of diamond and α -carbon layers with decreasing undercooling. Thus, amorphous carbon can be converted into diamond or Q-carbon followed by diamond or α -carbon.

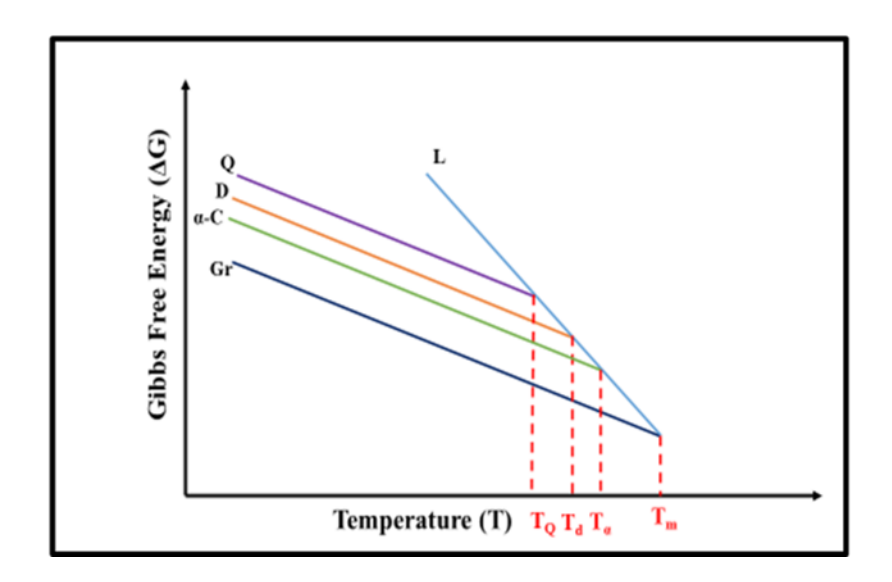


Fig. 1: Gibbs free energy versus temperature for graphite, α -carbon, diamond, Q-carbon, and liquid carbon with higher slope due to higher entropy.

Fig 1 illustrates the Gibbs free energy (ΔG) versus temperature (T), where free energy curves for graphite (equilibrium phase) and nonequilibrium phases (α -carbon, diamond, and Q-carbon) are intersected by molten carbon which has a higher entropy. The formation of different phases occurs at the free-energy intersections, where the degree of undercooling is taken to be the difference between the melting point of graphite (\sim 5000K) and the melting points of the different phases. When a thin layer of amorphous carbon (a-carbon) is melted in a super undercooled state, it can

lead to the formation of either 1) nanodiamonds in α -carbon and Q-carbon by homogeneous nucleation, 2) microdiamonds on sapphire substrate by heterogeneous nucleation, and 3) microdiamonds with Q-carbon near the sapphire interface, as shown schematically in Fig. 2 (a). Fig. 2(b) shows experimental results, where nanodiamonds are formed by homogeneous nucleation in α -carbon (R₁), and microdiamonds by heterogeneous nucleation at the sapphire interface (R₂). The formation of microdiamonds associated with Q-carbon is shown at R₃, where the number density is much higher than that at R₂. These microdiamonds formed with sapphire template grow epitaxially via domain matching epitaxy [15]. From the EBSD pattern (in the inset in Fig 2. (b)), the epitaxial relation on sapphire (0001) was determined to be <111> diamond //<0001> sapphire out of plane, and <110> diamond // <-2110> sapphire in-plane direction. Fig. 2(c) shows a direct comparison of diamond nucleation in α-carbon and Q-carbon. The Q-carbon provides easy nucleation sites for diamond growth, the details of which will be discussed later in the paper. It is interesting to note that microdiamonds grew directly on sapphire substrates without Q-carbon (at R₂) show a brighter contrast as a result of charge accumulation and enhanced electron emission during SEM imaging, compared to those grown with Q-carbon (at R₃). This is because Q-carbon is more conducting than sapphire [12]. It should be noted that the formation of circular Q-carbon regions (marked as R₃ in Fig 2(c)) of 2.5µm radius promotes the rapid growth of large <111> epitaxial diamond (2.0 μm) with an estimated growth velocity of over 5.0ms⁻¹. Similar growth of defect-free silicon with velocities over 1.0-2.0ms⁻¹ and dopant incorporation beyond the thermodynamic solubility limit via pulsed laser annealing as demonstrated in our earlier studies [16].

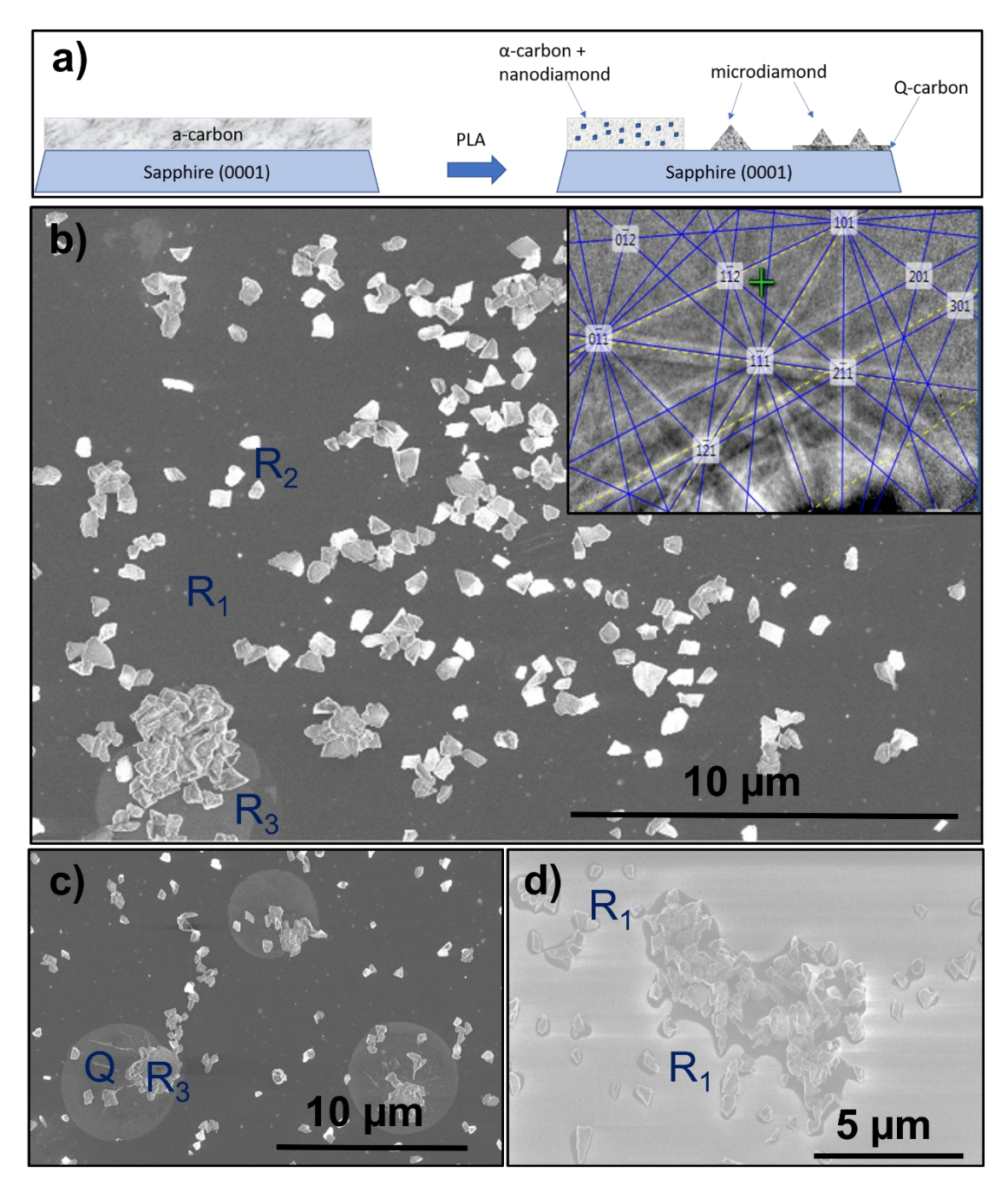


Fig. 2: (a) Schematic of conversion of a-carbon layer into nanodiamonds, microdiamonds, Q-carbon and quenched-in α -carbon; (b) formation of nanodiamonds by homogeneous nucleation at R_1 , microdiamonds by heterogeneous nucleation (R_2) in α -carbon; and much higher density of microdiamond nucleation in Q-carbon at R_3 . The inset EBSD shows epitaxial relation with (0001) sapphire substrate; (c) formation of circular Q-carbon regions, promoting diamond growth; and (d) formation of microdiamonds on (0001) sapphire and shrinkage associate with the diamond formation.

Fig. 2(d) shows the formation of individual and cluster microdiamonds on the sapphire (0001) interface by heterogeneous nucleation (R₁). It is interesting to note that there is a considerable shrinkage around diamond crystallites because the number density of carbon atoms in diamond is considerably higher than that in amorphous carbon. From the ratio surface areas (at (R₁), the density of diamond is estimated to be 50% higher than that of a-carbon. This is consistent with HAADF (STEM-Z) contrast ratio measurements, which is directly proportional to the atomic number density [13, 14]. In the presence of Q-carbon, the number density of microdiamonds is considerably higher due to an increase in the nucleation density of diamond.

The nucleation of diamonds occurs readily in the presence of Q-carbon, leading to the formation of a high density of microdiamonds, as demonstrated in Fig. 3. The experimental results in Fig. 3(a) clearly show the formation of nanodiamonds by homogeneous nucleation at R₁, microdiamonds by heterogeneous nucleation at R₂, and a much higher density of macrodiamonds in the presence of Q-carbon at R₃. Again the microdiamonds, which grow around Q-carbon, clearly show a darker contrast compared to those directly formed on sapphire (0001) due to the greater charge accumulation on the diamond in direct contact with insulating sapphire (0001) substrate. Fig 3(b) shows the formation of the continuous diamond film in the presence of Q-carbon and a comparison in the absence of Q-carbon. The sharp boundary clearly illustrates the role of Q-carbon in enhancing the number density of microdiamonds that coalesce to form a continuous diamond film. Fig. 3(c) shows the formation of continuous diamond over the entire substrate surface in the presence of a Q-carbon interposing layer. Preliminary scotch-tape and scratch tests showed that these films are highly adherent presumably due to the presence of the interposing layer of Q-carbon, as shown in Fig. 3(c) [17].

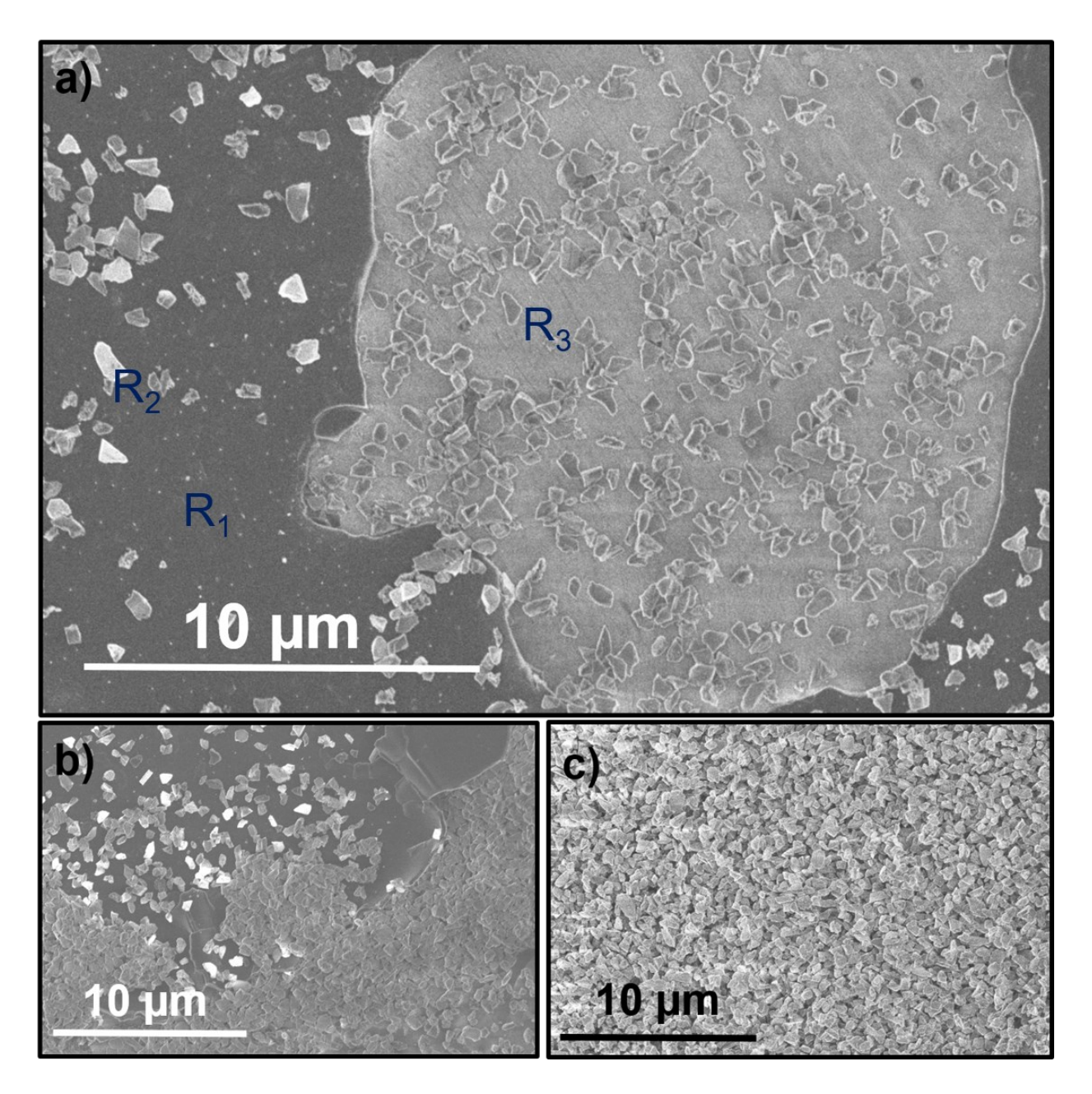


Fig 3: (a) Formation of larger regions of Q-carbon with increasing number density of microdiamonds on Q-carbon; (b) highlights the role of Q-carbon in diamond nucleation and formation of continuous and adherent diamond films on sapphire and glass substrates; and (c) continuous adherent microdiamond film.

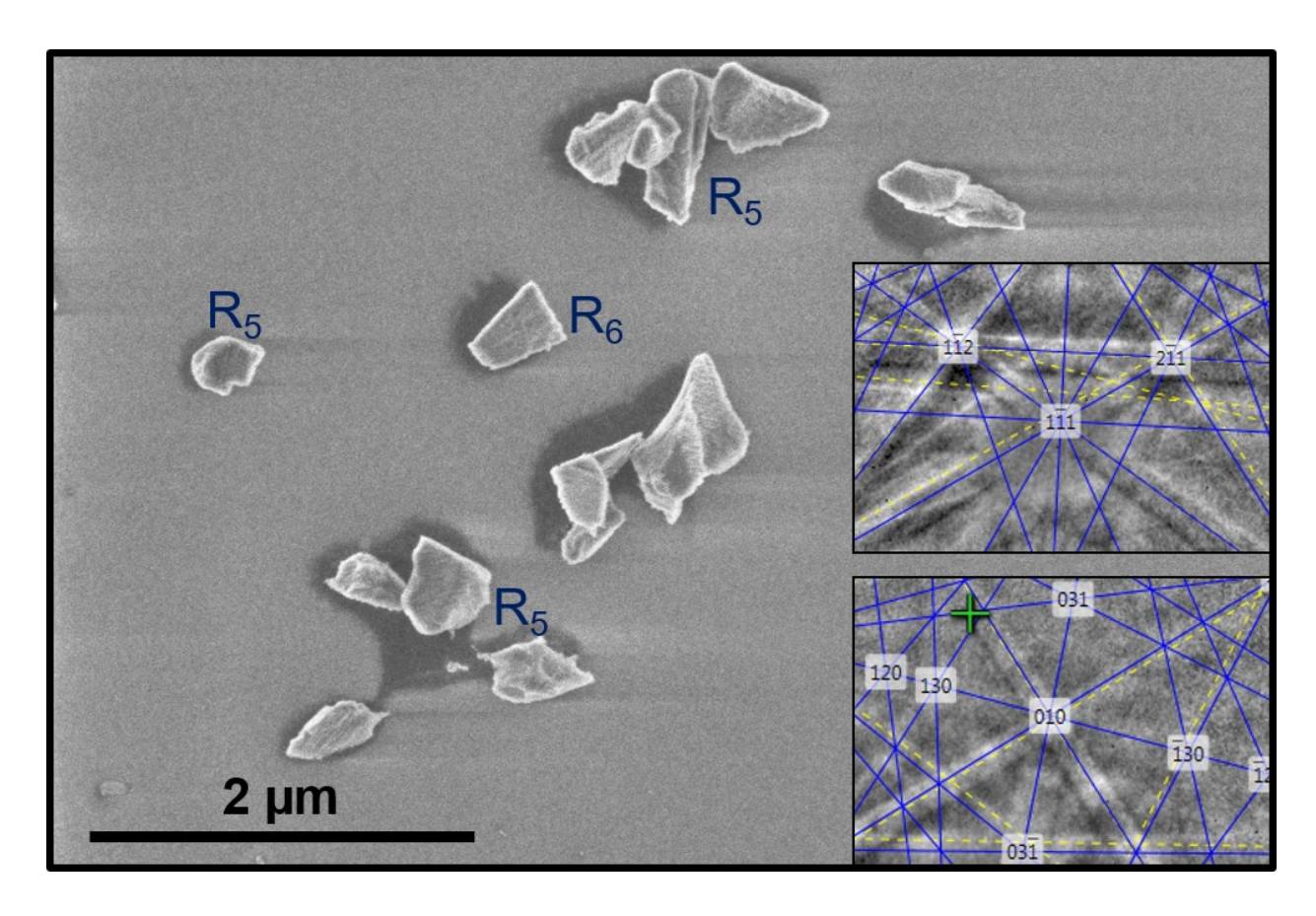


Fig 4: HRSEM micrographs of microdiamonds in <111> (at R_5) and in <100> orientation (at R_6) with inset showing EBSD for <111> and <100> orientations.

The details of epitaxial growth of diamond is illustrated in Fig. 4, where <111> and <100> diamond epitaxy is shown at R_5 and R_6 , respectively. The epitaxial growth is confirmed by corresponding EBSD patterns for <111> and <100> growth in the insets of Fig. 4. By comparing with sapphire (0001) EBSD, the epitaxial relations for <111> diamond growth are <111> diamond // <0001> Sapphire out of the plane, and <110> diamond // < $\overline{2}110$ > Sapphire in the plane. The epitaxial relations for <100> diamond growth are <100> diamond // <0001> Sapphire out of the plane, and <110> diamond // <100> diamond // <100> Sapphire in one direction, and <110> diamond // <1010> Sapphire in the other direction of the plane. The relative fraction of <111> and <100> oriented

diamond crystallites can be controlled through crystallization kinetics by optimizing the laser parameters.

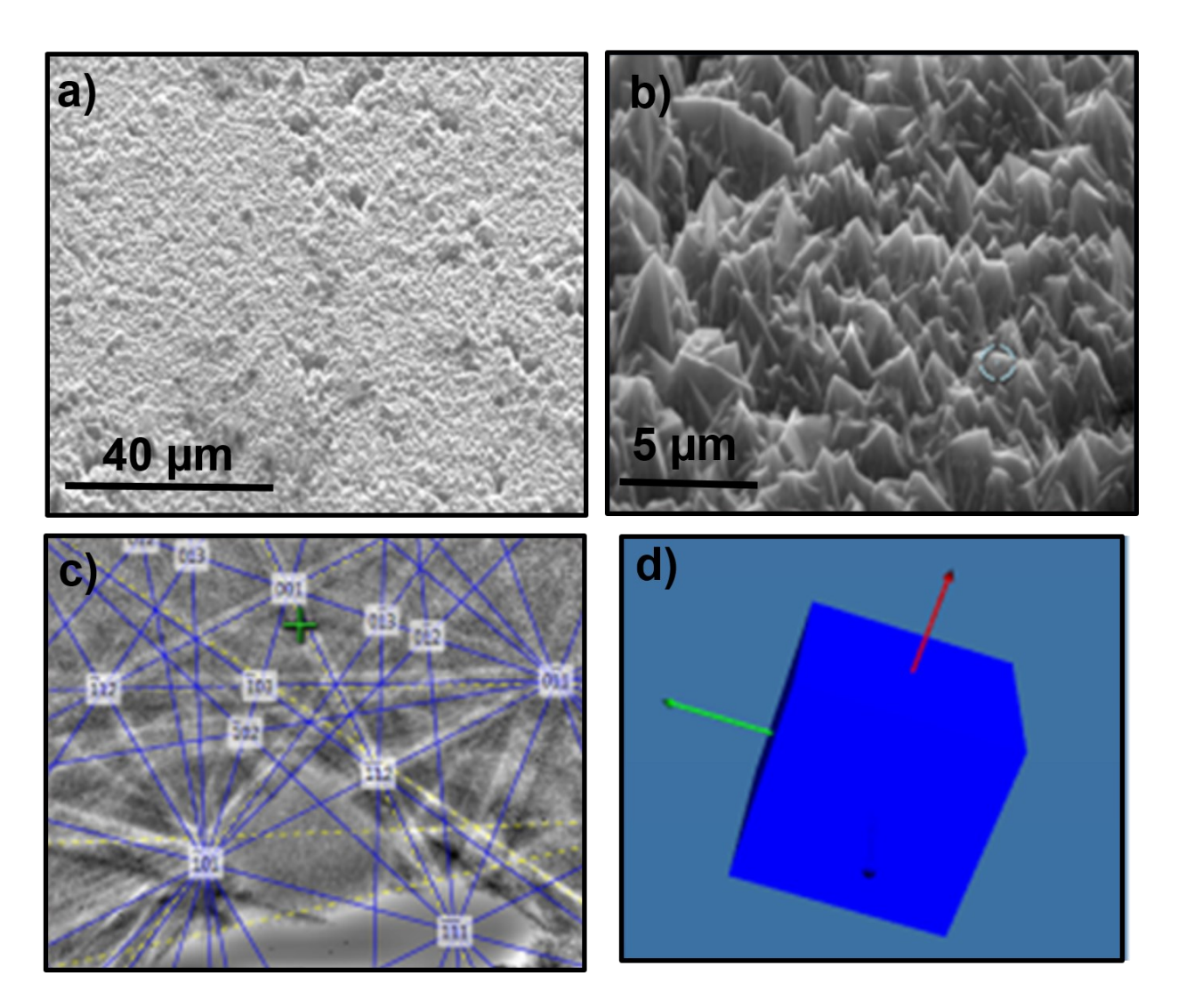


Fig. 5: (a) Continuous diamond film on Q-carbon seeding and HFCVD for 3 hours; (b) SEM micrograph at a higher resolution; (c) EBSD pattern showing <100> diamond growth; and (d) relative <100> orientation.

The effectiveness of Q-carbon layer in providing nucleation sites for diamond growth by HFCVD is illustrated in Fig. 5. The SEM micrograph in Fig. 5(a) shows the formation of a continuous <100> textured diamond film on the Q-carbon coated sapphire substrate after three hours of HFCVD growth on (0001) sapphire. Here the diamond nuclei are formed near the top of Q-carbon,

therefore, <100> texturing occurs as a result of faster diamond growth in <100> direction, compared to <110 and <111> during HFCVD. Whenever, the diamond nucleation is at the Q-carbon/substrate interface, the growth orientation is dictated by the substrate orientation and domain matching epitaxy. Fig. 5(b) shows the details of morphology at a higher magnification and <100> orientation of microdiamonds, as shown in Fig. 5(b) and 5(c). It should be mentioned that without Q-carbon seeding, only a few diamond crystallites are observed after three hours of HFCVD growth [17].

The nucleation of diamond on glass presents a similar challenge as on sapphire due to the lack of surface affinity with carbon, similar to sapphire in the CVD temperature range. As a result, nucleation of diamond and growth of continuous films on glass substrates by CVD has proven quite difficult. Fig. 6(a) shows a high-density nucleation of microdiamonds in the presence of Q-carbon on a glass substrate. This micrograph shows a significant enhancement in diamond nucleation over the entire substrate surface in the presence of the interposing Q-carbon layer. The contrast from the top diamond layer is lighter (more insulating) compared to the layer underneath, which grows directly on Q-carbon. Thus, Q-carbon can be used to form a continuous film on a glass substrate, as shown in Fig. 6(b). The effectiveness of Q-carbon in nucleation and formation of a continuous thin film over a large area are illustrated clearly in Fig. 6(c). There is no diamond growth to be seen on glass substrates in the absence of Q-carbon, whereas a very dense continuous film is observed in the presence of Q-carbon.

The Raman measurements show that these microdiamonds and continuous films on sapphire have the characteristic T_{2g} peak close to 1332 cm⁻¹, as shown in Fig. 7(a). This implies that the microdiamond films are fairly stress-free. In the case of nanodiamonds, there is a downshift (to 1325 cm⁻¹) associated with phonon-confinement effects [18], as shown in Fig. 7(b). The lack of

thermal stress in these diamond films can be explained if the underlying does not heat to high temperatures or the interposing Q-carbon layer has a matching thermal expansion coefficient with the diamond. Thermal strains are given by $\varepsilon_T = \alpha_f (T_f - T_0) - \alpha_s (T_s - T_0)$, where α_f and α_s are coefficients of thermal expansion and T_f and T_s are effective temperatures of diamond and sapphire, respectively, during laser processing. By using an average values of $\alpha_s = 6.0 \times 10^{-6} \text{K}^{-1}$ for sapphire and $\alpha_f = 1.0 \times 10^{-6} \text{K}^{-1}$ for diamond, the quenching from $T_f = 4000 \text{K}$ can generate negligible strain with sapphire temperature of 916K). The temperature of 916K for sapphire substrate was estimated by laser-solid interaction calculations using the SLIM program [19]. The corresponding thermal stress is given by $\sigma_T = 2\mu\varepsilon_T \left[(1-\upsilon)/(1+\upsilon) \right]$ will also be also very small, where μ (555 GPa) and υ (0.1) are shear modulus and Poisson's ratio of the diamond, respectively.

Microdiamonds nucleate more efficiently at α -carbon/sapphire and Q-carbon/sapphire interfaces due to the higher undercooling and thus greater negative Gibbs free energy. The Gibbs free energy for diamond nucleation from the undercooled carbon melt is given by $\Delta G_T = -\Delta H_m$. $\Delta T/T_m$, where ΔT is the undercooling, ΔH_m the melting enthalpy, and T_m is the melting point of carbon. Since the undercooling is higher at Q-carbon/sapphire interface, the number density of diamond nuclei is higher at the Q-carbon/sapphire than α -carbon/sapphire interface. However, the average size of microdiamond is roughly the same at both the α -carbon/sapphire and Q-carbon/sapphire interfaces, because the diamond growth time are approximately equal.

Fig. 8 shows the results of laser-solid interaction calculations using the SLIM program on sapphire substrates [19]. The figure shows the plot of temperature versus time (Fig. 8(a)), melt depth versus time (Fig. 8(b)), and melt growth velocity as a function of time (Fig. 8(c)). The melt-growth velocity varies from 2-4 ms⁻¹, which can lead to the formation of 0.5-1.0 μm microdiamonds in about 200ns of growth time in the liquid phase. The growth rates of Q-carbon in the form of

circular patches (shown in Fig. 3 (c)) are considerably higher (2-3 times) than diamond, which is consistent with SLIM calculations.

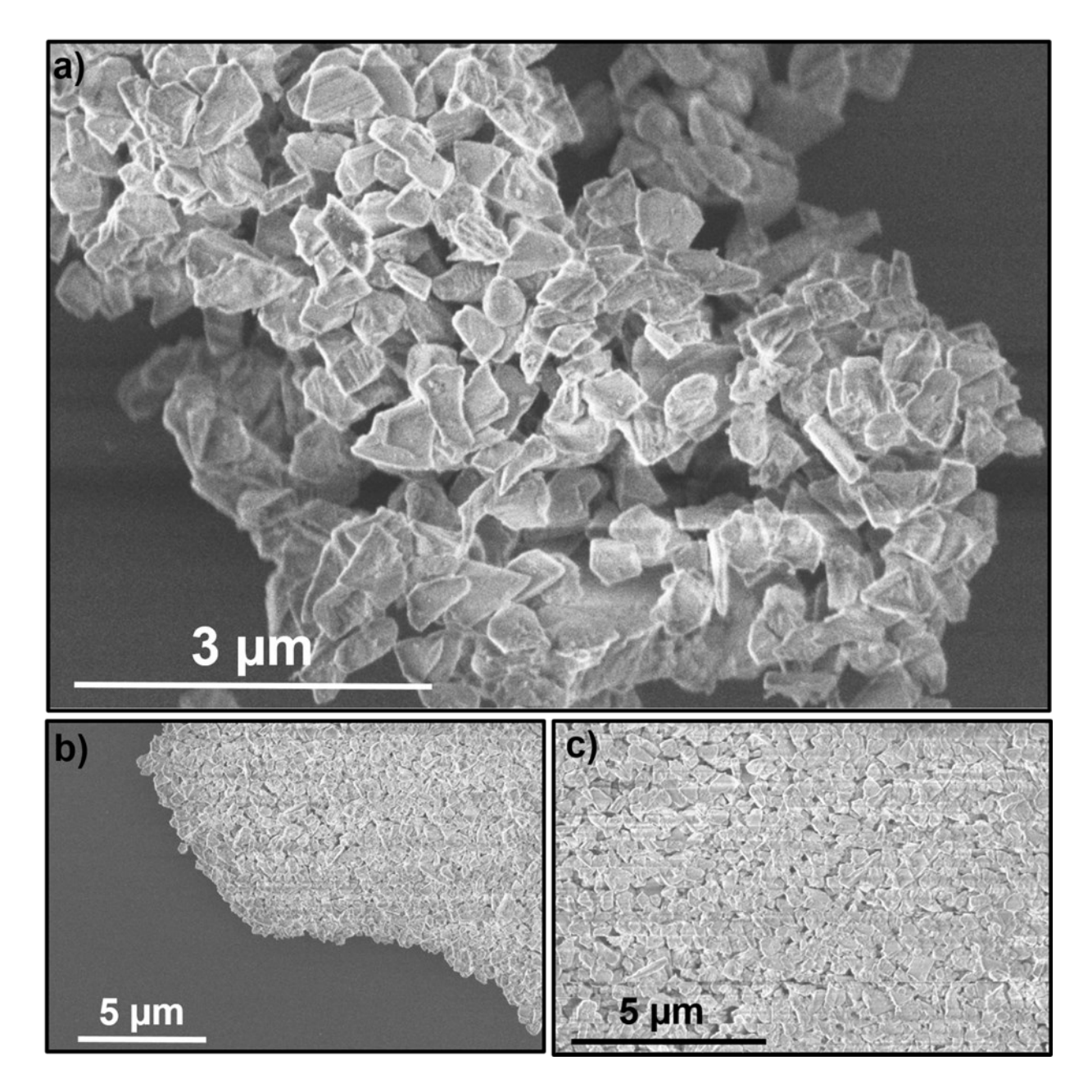


Fig. 6: (a) Enhanced nucleation and growth of diamond on glass in the presence of Q-carbon; (b) boundary between a continuous film with Q-carbon and without Q-carbon; and (c) continuous adherent diamond film on the glass substrate.

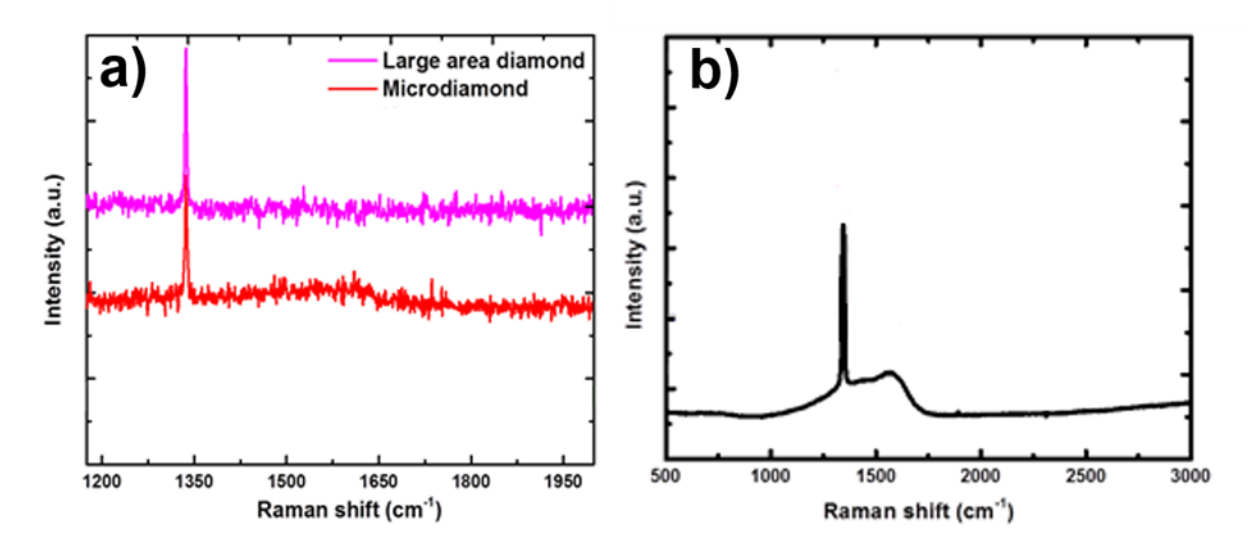


Fig. 7: (a) Raman spectra from microdiamonds (peak at 1332 cm⁻¹); and (b) Raman spectra from nanodiamonds (peak at 1325 cm⁻¹).

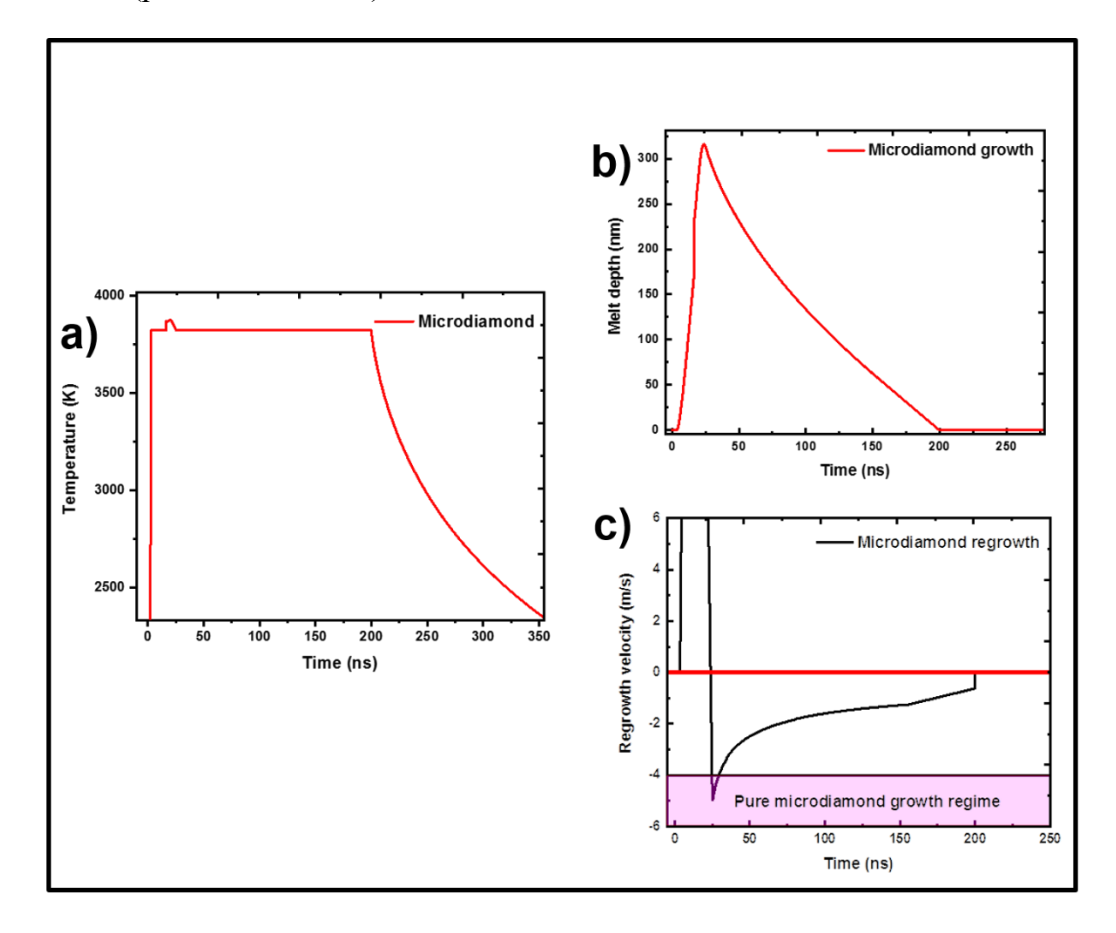


Fig. 8: SLIM simulation results: (a) Temperature versus time; (b) Melt depth versus time; (c) melt-growth velocity versus time.

The structure of Q-carbon has been analyzed in considerable detail in the context of high-temperature superconductivity. Three distinct phases have been identified in B-doped Q-carbon, namely, Q_{B1} , Q_{B2} , and Q_{B3} [20], consistent with theoretical predictions by Cohen's group [21]. It should be mentioned that the formation of Q-carbon after laser annealing of amorphous carbon has been independently confirmed by Yoshinaka et al [22]. The Q_{B1} phase is formed when only one of the three tetrahedra, joined along the edges as shown in Fig. 9(a), are doped with B (central blue atom), and these units are randomly packed upon quenching with >80% packing efficiency.

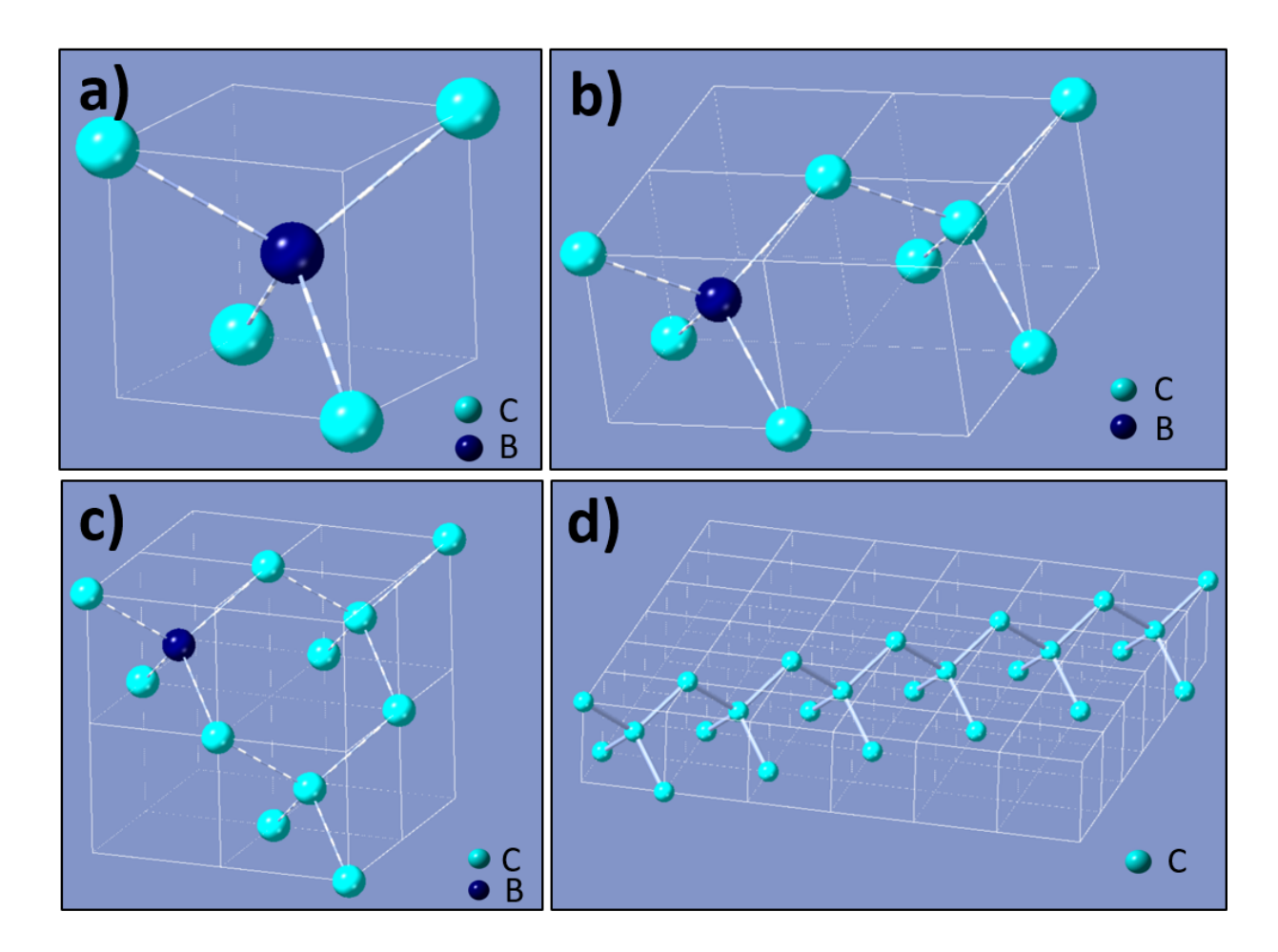


Fig. 9: Atomic structure of Q-carbon: (a) Q₃-phase; (b) Q₂; (c) Q₁ phase; and (d) tetrahedra align along <110> to form string-like structures.

This phase, with 17at%B exhibits a superconducting transition temperature of 37K. When two tetrahedra, joined along the edges as shown in Fig 9(b), are packed randomly upon quenching, Q_{B2} phase is formed. If one of the two tetrahedra contains B, this phase will have 25%B. This phase has shown a superconducting transition temperature of 55K, which is the highest transition temperature for the BCS superconductivity. The Q_{B3} phase is formed when tetrahedra with central B atoms are packed with resulting 50%B concentration, as shown in Fig. 9(c). These tetrahedral structures in doped and undoped Q-carbon phases are formed in a super undercooled state and play a critical role in the easy nucleation of the diamond phase. These tetrahedra can organize themselves as strings [23], whose lengths increase with increasing undercooling. Fig. 9(d) shows diamond tetrahedra joined along <110> direction to create a string-like structure. It is surmised that clusters of diamond tetrahedral in Q-carbon have exceeded that critical size for diamond nucleation [24, 25].

The atomic structure and bonding characteristics of Q-carbon on sapphire were analyzed in detail by annular dark-field imaging, selected area electron diffraction (SAED), and electron energy-loss spectroscopy techniques. Figure 10(a) shows a cross-sectional annular dark-field image of Q-carbon on sapphire c-Al₂O₃ substrate, where the thickness of Q-carbon is estimated to be ~50 nm. A selected area electron diffraction (SAED) pattern (Fig. 10(b)), obtained on Q-carbon, shows a diffused ring pattern, revealing the amorphous nature of Q-carbon. The spectrum contains diffused, but distinct (111) and (220) diffraction rings in the SAED pattern, indicating the presence of sp³ bonded carbon tetrahedra in Q-carbon structure. This is consistent with the proposed atomic structure proposed in Fig. 9, where the diamond tetrahedra are randomly packed to create the densely packed phase of Q-carbon. However, more work is needed to distinguish between Q₁, Q₂ and Q₃ phases.

The electronic structure across the Q-carbon layer was analyzed by mapping out EELS spectra. The Q-carbon EELS spectrum consists of peaks at C-K (284 eV) and O-K (532 eV), corresponding to high spectral counts shown in Fig. 10(c). The sudden rise in O-K peak intensity at the interface between Q-carbon and Al₂O₃ suggests the formation of an atomically-sharp interface between Qcarbon and the substrate following the ultrafast quench. An enlarged spectrum image between 275 and 310 eV is shown in Fig. 10(d), with the details of the C-K edge. The spectrum clearly shows the presence of π^* (onset at 284 eV) and σ^* (broad peak with onset at 290 eV) excited states in the C-K edge, thus revealing the presence of both the sp² and sp³ bonded carbon atoms in Q-carbon. The sp³ and sp² content in Q-carbon was quantified using a Gaussian fit method [5, 26] as shown in Fig. 10(d). The C-K edge is fitted with three major Gaussian profiles which attribute to C=C π^* (285 eV), C=C σ^* (292 eV) and C-C σ^* (298 eV). One additional small Gaussian peak at 287 eV was also added to appropriately fitting the C-K edge, which is attributed to the non-planar contribution of π^* . Using these fits, we estimated 80 ± 2 % sp³ in Q-carbon, which is in agreement with the sp³ fraction determined by using quantitative Raman spectroscopy (~82% sp³). The Q-carbon is strongly adherent to sapphire because of its interfacial reaction with the substrate, as discussed below. Adhesion of diamond films without any interfacial reactions is usually poor [1,2]. The Gibbs free energy for the reaction of solid carbon with alumina is positive up to fairly high temperatures. In the case of sapphire, the reaction of carbon to form aluminum carbide can occur only at very high temperatures, close to the melting point when the Gibbs free energy turns negative. The reaction with liquid carbon can occur at 4000K, as Gibbs free energy turns negative, and high-diffusivity in the liquid can lead to the formation of interfacial aluminum carbide (Al₄C₃) rapidly within 100ns. The Gibbs free energy versus calculations are shown in Fig. 11, where it turns negative with molten carbon. It is believed that this reaction is responsible for the observed improved adhesion in our films.

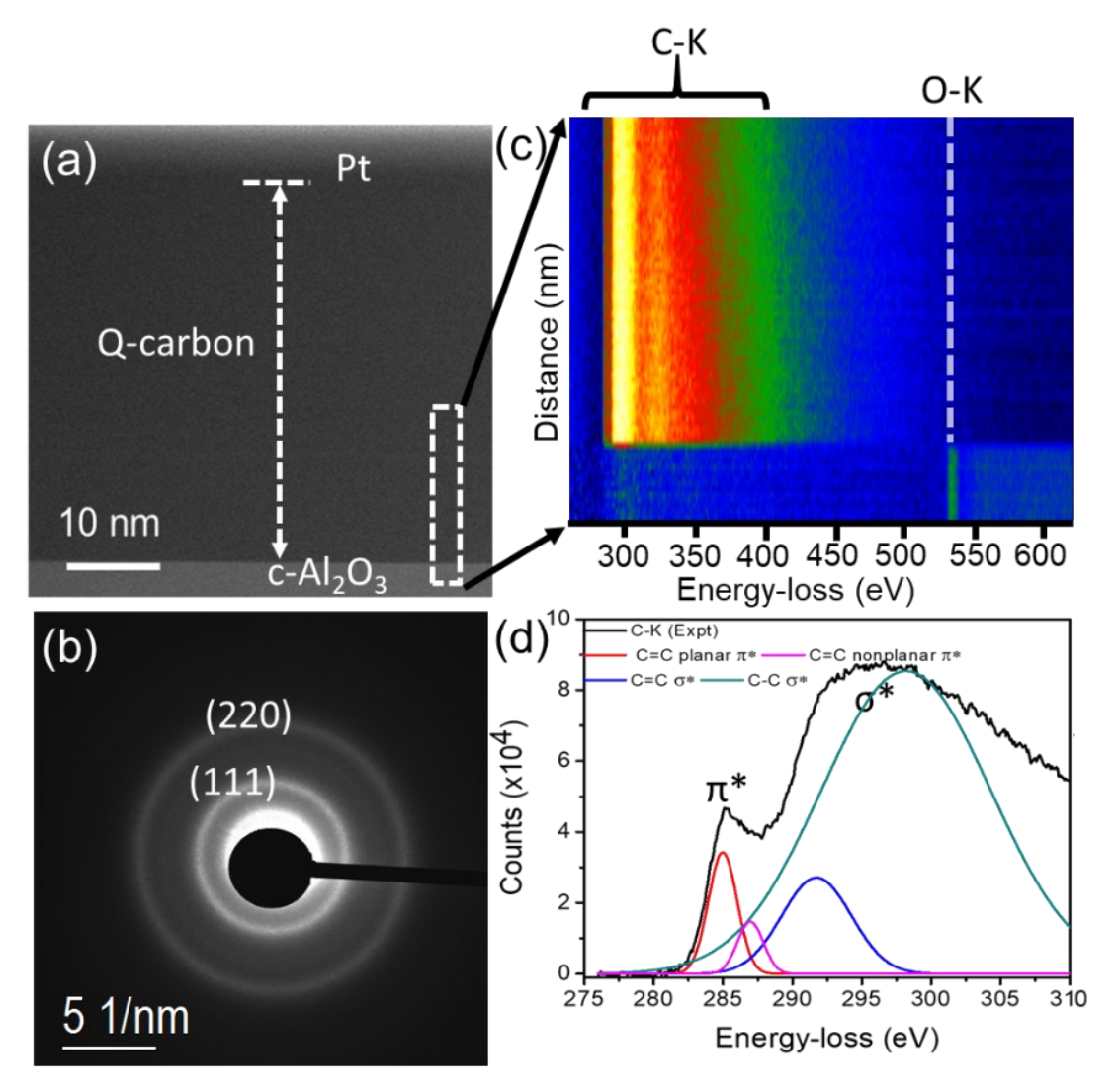


Fig.10. (a) A cross-sectional ADF image of Q-carbon on c-sapphire substrate. (b) SAED pattern of Q-carbon showing diffused diffraction rings corresponding to amorphous structure, (c) reveals the EEL spectral acquisitions across the Q-carbon/Al₂O₃ heterostructure, highlighting the C and O elemental mapping (d) Gaussian fitted EELS spectrum of Q-carbon region revealing the constituent π^* and σ^* peaks in C-K edge of Q-carbon.

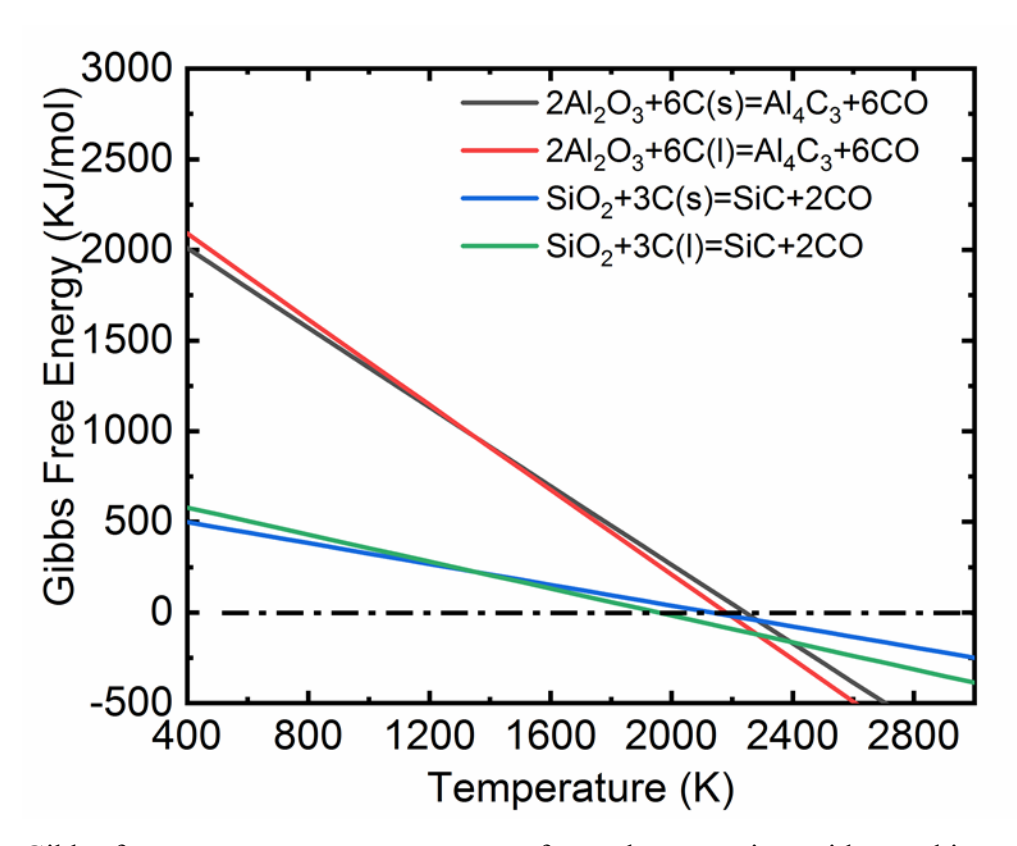


Fig. 11: Gibbs free energy versus temperature for carbon reaction with sapphire; and carbon reaction with glass.

Comparison between (liquid-phase) laser processing and (solid state) BEN MPCVD

The negative substrate biasing works very effectively in enhancing the nucleation sites under microwave plasma CVD. Under negative biasing, it is surmised that positively charged Hx+, Cx+, CHx+ species impinge upon the substrate and stabilize sp³ bonded diamond nuclei. The negative biasing also works for HFCVD, provided there are positively plasma species. Some have argued that biasing modifies the plasma chemistry and enhances carbide formation on the substrate [7]. Schreck and colleagues [10] have taken all these biased enhanced nucleation results and provided a model which focuses on domain formation and ion-bombardment-induced-buried lateral growth, but the model requires excessive displacement damage to account for their observed growth rates.

Finally, we discuss similarities between biased enhanced nucleation (BEN) during MPCVD and laser-enhanced nucleation (LEN) during direct conversion of carbon into diamond by pulsed laser annealing. As shown in Figs. 2(b), (c), and 3, the formation of Q-carbon is responsible for enhanced nucleation of diamond nuclei which grow into large epitaxial microdiamonds. These microdiamonds can grow epitaxially by matching of plane between the diamond film and the substrate via domain matching epitaxy paradigm. The formation of circular structures, referred as domains, during the application bias in MPCVD (Fig 1 (a)) in reference [9] is shown in Fig. S2 for a comparison. These domains in Fig. S2 are very similar to circular Q-carbon structures in the present LEN (Figs. 2(b), (c) and 3). The size of these circular Q-carbon regions is of the order of 3-6µm, which are formed within 100-200ns during pulsed laser annealing by ArF laser with 20ns pulse duration. These regions grow from the substrate with an undercooled liquid-phase velocity of over 5.0ms-1 having a first-order phase transformation. Under the BEN, the transformation of Q-carbon layer 1-2nm thick under solid-state phase transformation may take seconds, considering solid-phase epitaxial growth in amorphous silicon. We propose that during the application of bias in MPCVD, amorphous carbon layer is formed, which is continuously bombarded by Hx+, CHx+ ions having an energy of ~250eV (bias voltage times charge). This energy of a CHx+ ion can generate two Frenkel (vacancy-interstitial) pairs per ion, which can convert three-atom covalently bonded units into a five-atom diamond tetrahedron, as shown in Fig. 9(a). The number of Frenkel pairs (NFP) under low-energy bombardment can be estimated by NFP = $0.8x4M_1M_2x(M_1+M_2)$ -2xE_i/(2E_d), where M₁ is mass of the incident ion, M₂ is mass of substrate, E_d is damage threshold energy, and E_i is the energy of incident ion [27]. Thus there is a bias threshold for BEN to work efficiently, above which excessive damage would prevent the formation of sp³ DCL tetrahedra. These diamond tetrahedra get compacted with over 80% efficiency to form Q-carbon and its

different polymorphs. In the case of MPCVD on Ir substrates, the Ir(100) provides a template for diamond epitaxy with 7.1% lattice misfit which can be handled by domain matching epitaxy. KPFM measurements showed negative surface potential associated with Q-carbon compared to the matrix of diamond and diamond-like carbon [12], which is similar to reduced work function associated with domains after the BEN treatment [9]. A significant shrinkage and increase in the mass density of Q-carbon (>50%) was found by using HAADF (STEM-Z) contrast, which is directly proportional to the atomic number density. This is consistent with significant shrinkage >50% of bright domain regions compared to as-deposited carbon regions in BEN experiments.

4. Summary

We have solved a longstanding challenge related to diamond nucleation and fabrication of continuous and epitaxial diamond films on nondiamond substrates for next-generation solid state devices involving diamond thin film heterostructures. We have shown that a new phase of carbon, named Q-carbon, provides ready nucleation sites and these nuclei can be grown subsequently by laser processing, HFCVD or MWCVD to form continuous diamond films over a large area for a wafer-scale integration. By controlling the diamond nucleation near the Q-carbon/substrate interface, we can achieve epitaxial growth of diamond film with the substrate acting as a template. The heterogeneous nucleation is favored over homogeneous nucleation, and further manipulated by reducing the Q-carbon layer thickness. We have shown that the Q-carbon layers can be produced by nanosecond laser melting and subsequent quenching in a controlled way. Using nanosecond lasers, the whole conversion process from amorphous into Q-carbon is completed in less than fraction of a microsecond. Each pulse creates about one square cm which can be scaled up to cover 100 to 200 square cm by using 100-200Hz laser.

We also argue that biased enhanced nucleation under MWCVD is a result of formation of thin Q-carbon layer. This thin Q-carbon layer is formed under a delicate balance of sputtering and displacement damage during the intense flux of CxHy+ ions with energy equal to charge times the bias voltage. These domains of Q-carbon layer provide effective nucleation sites for diamond growth subsequently with bias turned off. This Q-carbon layer provides enhanced nucleation sites for epitaxial diamond film with crystalline substrate such as Ir (100) via domain matching epitaxy or random diamond film with amorphous substrate such as glass or SiO₂/Si. These non-carbide forming substrates usually exhibit very poor nucleation and adhesion for CVD growth processes. Improved adhesion can be derived by interfacial reaction of liquid carbon with glass and sapphire at high temperatures, where Gibbs free energy turns negative facilitating interfacial carbide formation. This transformative research on adherent Q-carbon and diamond coatings on nondiamond substrates will have a profound impact on the fundamental understanding of formation of continuous adherent diamond films on non-carbide forming substrates.

Acknowledgment

The authors are pleased to acknowledge stimulating discussions with Professor John Prater and useful comments on the manuscript. This work was supported by the National Science Foundation Grant (DMR-2016256).

References:

- [1] D. Das, R.N. Singh, A review of nucleation, growth and low temperature synthesis of diamond thin films, Int. Mater. Rev. 52 (2007) 29–64. https://doi.org/10.1179/174328007X160245.
- [2] H. Liu, D.S. Dandy, Studies on nucleation process in diamond CVD: an overview of recent developments, Diam. Relat. Mater. 4 (1995) 1173–1188. https://doi.org/10.1016/0925-9635(96)00297-2.
- [3] C.E. Nebel, B. Rezek, D. Shin, H. Uetsuka, N. Yang, Diamond for bio-sensor applications, J. Phys. D. Appl. Phys. 40 (2007) 6443–6466. https://doi.org/10.1088/0022-3727/40/20/S21.
- [4] R.K. Singh, D.R. Gilbert, J. Fitz-Gerald, S. Harkness, D.G. Lee, Engineered Interfaces for Adherent Diamond Coatings on Large Thermal- Expansion Coefficient Mismatched Substrates, Science (80). 272 (1996) 396–398. http://www.istor.org/stable/2890316
- [5] R. Sachan, A. Bhaumik, P. Pant, J. Prater, J. Narayan, Diamond film growth by HFCVD on Q-carbon seeded substrate, Carbon 141 (2019) 182–189. https://doi.org/10.1016/j.carbon.2018.09.058.
- [6] S. Yugo, T. Kanai, T. Kimura, T. Muto, Generation of diamond nuclei by electric field in plasma chemical vapor deposition, Appl. Phys. Lett. 58 (1991) 1036–1038. https://doi.org/10.1063/1.104415.
- [7] B.R. Stoner, G.H.M. Ma, S.D. Wolter, J.T. Glass, Characterization of bias-enhanced nucleation of diamond on silicon by invacuo surface analysis and transmission electron microscopy, Phys. Rev. B. 45 (1992) 11067–11084. https://doi.org/10.1103/PhysRevB.45.11067.

- [8] K. Ohtsuka, K. Suzuki, A. Sawabe, T. Inuzuka, Epitaxial growth of diamond on iridium, Japanese J. Appl. Physics, Part 2 Lett. 35 (1996). https://doi.org/10.1143/jjap.35.11072.
- [9] M. Schreck, T. Bauer, S. Gsell, F. Hörmann, H. Bielefeldt, B. Stritzker, Domain formation in diamond nucleation on iridium, Diam. Relat. Mater. 12 (2003) 262–267. https://doi.org/10.1016/S0925-9635(02)00361-8.
- [10] M. Schreck, S. Gsell, R. Brescia, M. Fischer, Ion bombardment induced buried lateral growth: The key mechanism for the synthesis of single crystal diamond wafers, Sci. Rep. 7 (2017) 1–8. https://doi.org/10.1038/srep44462.
- [11] R. N. Singh (to be published). J. Narayan, A.R. Srivatsa, M. Peters, S. Yokota, K. V. Ravi, On epitaxial growth of diamond films on (100) silicon substrates, Appl. Phys. Lett. 53 (1988) 1823–1825. https://doi.org/10.1063/1.99791.
- [12] J. Narayan, A. Bhaumik, Novel phase of carbon, ferromagnetism, and conversion into diamond, J. Appl. Phys. 118 (2015). https://doi.org/10.1063/1.4936595.
- [13] S. Gupta, R. Sachan, A. Bhaumik, P. Pant, J. Narayan, Undercooling driven growth of Q-carbon, diamond, and graphite, MRS Commun. 8 (2018) 533–540. https://doi.org/10.1557/mrc.2018.76.
- [14] R. Sachan, S. Gupta, J. Narayan, Nonequilibrium Structural Evolution of Q-Carbon and Interfaces, ACS Appl. Mater. Interfaces. 12 (2020) 1330–1338. https://doi.org/10.1021/acsami.9b17428.
- [15] J. Narayan, B.C. Larson, Domain epitaxy: A unified paradigm for thin film growth, J. Appl.

- Phys. 93 (2003) 278. https://doi.org/10.1063/1.1528301.
- [16] C.W. White, J. Narayan, R.T. Young, Laser annealing of ion-implanted semiconductors, Science (80). 204 (1979) 461–468. https://doi.org/10.1126/science.204.4392.461.
- [17] P. Joshi, S. Gupta, A. Haque, J. Narayan, Fabrication of ultrahard Q-carbon nanocoatings on AISI 304 and 316 stainless steels and subsequent formation of high-quality diamond films, Diam. Relat. Mater. 104 (2020) 107742. https://doi.org/10.1016/j.diamond.2020.107742.
- [18] S. Prawer, R.J. Nemanich, Raman spectroscopy of diamond and doped diamond, Philosophical Transactions of the Royal Society of London. Series A: Mathematical, Physical and Engineering Sciences 362 (2004) 2537–2565. https://doi.org/10.1098/rsta.2004.1451.
- [19] R.K. Singh, J. Narayan, A novel method for simulating laser-solid interactions in semiconductors and layered structures, Mater. Sci. Eng. B. 3 (1989) 217–230. https://doi.org/10.1016/0921-5107(89)90014-7.
- [20] J. Narayan, A. Bhaumik, R. Sachan, High temperature superconductivity in distinct phases of amorphous B-doped Q-carbon, J. Appl. Phys. 123 (2018) 135304. https://doi.org/10.1063/1.5016397.
- [21] Y. Sakai, J.R. Chelikowsky, M.L. Cohen, Simulating the effect of boron doping in superconducting carbon, Phys. Rev. B. 97 (2018). https://doi.org/10.1103/PhysRevB.97.054501.
- [22] H. Yoshinaka, S. Inubushi, T. Wakita, T. Yokoya, Y. Muraoka, Formation of Q-carbon by adjusting sp³ content in diamond-like carbon films and laser energy density of pulsed laser annealing, Carbon N. Y. 167 (2020) 504–511. https://doi.org/10.1016/j.carbon.2020.06.025.

- [23] C. Donati, J.F. Douglas, W. Kob, S.J. Plimpton, P.H. Poole, S.C. Glotzer, Stringlike cooperative motion in a supercooled liquid, Phys. Rev. Lett. 80 (1998) 2338–2341. https://doi.org/10.1103/PhysRevLett.80.2338.
- [24] R.F. Wood, D.H. Lowndes, J. Narayan, Bulk nucleation and amorphous phase formation in highly undercooled molten silicon, Appl. Phys. Lett. 44 (1984) 770–772. https://doi.org/10.1063/1.94912.
- [25] D.H. Lowndes, R.F. Wood, J. Narayan, Pulsed-Laser Melting of Amorphous Silicon: Time-Resolved Measurements and Model Calculations, Phys. Rev. Lett. 52 (1984) 561–564. https://doi.org/10.1103/PhysRevLett.52.561.
- [26] R. Sachan, J.A. Hachtel, A. Bhaumik, A. Moatti, J. Prater, J.C. Idrobo, J. Narayan, Emergence of shallow energy levels in B-doped Q-carbon: A high-temperature superconductor, Acta Mater. 174 (2019) 153–159. https://doi.org/10.1016/j.actamat.2019.05.013.
- [27] J. Narayan, O.W. Holland, Characteristics of Ion-Implantation Damage and Annealing Phenomena in Semiconductors, J. Electrochem. Soc. 131 (1984) 2651–2662. https://doi.org/10.1149/1.2115377.